

Machine Learning for the Cluster Reconstruction in the CALIFA Calorimeter at R3B

T. Jenegger^a, N. Hartman^a, R. Gernhäuser^a, L. Fabbietti^a, L. Heinrich^a

^a*TUM School of Natural Sciences, Technical University of Munich, Germany*

Abstract

The R3B experiment at FAIR studies nuclear reactions using high-energy radioactive beams. One key detector in R3B is the CALIFA calorimeter consisting of 2544 CsI(Tl) scintillator crystals designed to detect light charged particles and gamma rays with an energy resolution in the per cent range after Doppler correction. Precise cluster reconstruction from sparse hit patterns is a crucial requirement. Standard algorithms typically use fixed cluster sizes or geometric thresholds. To enhance performance, advanced machine learning techniques such as agglomerative clustering were implemented to use the full multi-dimensional parameter space including geometry, energy and time of individual interactions. An Edge Detection Neural Network exhibited significant differences. This study, based on Geant4 simulations, demonstrates improvements in cluster reconstruction efficiency of more than 30%, showcasing the potential of machine learning in nuclear physics experiments.

Keywords: R3B Experiment, CALIFA Calorimeter, Cluster Reconstruction, Machine Learning, Simulation

1. Introduction

With the advancements in facilities dedicated to the production of radioactive beams at relativistic energies, such as the Facility for Antiproton and Ion Research (FAIR) at GSI, significant progress is expected for our understanding of exotic nuclei far from stability [1]. FAIR will provide high-intensity relativistic radioactive beams of rare isotopes with energies in the range of 1 A

14 GeV, enabling investigations with full kinematic reconstruction [2]. A key ex-
 15 perimental setup designed for this purpose is the **R**eactions with **R**elativistic
 16 **R**adioactive **B**eams (R3B) setup, providing access to high-resolution spectro-
 17 scopic data. This setup serves as a unique tool for unveiling the structure of
 18 nuclei and their reaction dynamics with unprecedented precision.
 19 At the core of the R3B Setup is the CALIFA calorimeter (Calorimeter for the
 20 In-Flight Detection of Gamma Rays and Light Charged Particles), a highly
 21 segmented detection system composed of 2544 CsI(Tl) scintillator crystals that
 22 hermetically enclose the target area in the polar angular range of $7^\circ < \theta < 140^\circ$.
 23 This design enables the simultaneous measurement of gamma rays down to $E_\gamma \approx$
 24 100 keV and light charged particles, such as protons and deuterons, up to sev-
 25 eral hundred A MeV [3]. To ensure optimal performance, extensive research has
 26 been conducted to refine the geometric design, minimize scattering and energy
 27 loss due to the mechanical structure [4], and develop a dead-time-free data ac-
 28 quisition system capable of handling high-rate experiments [5]. Furthermore,
 29 a seamless integration within the R3BRoot framework [6] has been achieved,
 30 enabling offline data analysis from the raw to the calibrated data level and ul-
 31 timately to the cluster level, where individual hits are recombined for the final
 32 energy reconstruction.
 33 This study presents the results of a hierarchical machine learning model to en-
 34 hance the energy reconstruction of gamma rays in CALIFA. Using simulated
 35 Geant4 data, the performance of the geometrical R3B clustering algorithm is
 36 compared to an agglomerative clustering model [7] and a multi-layer perceptron
 37 architecture [8], demonstrating the potential of machine learning techniques in
 38 improving reconstruction efficiency and accuracy.

39

2. Methodology

2.1. Challenges in Relativistic Gamma Spectroscopy

While the detection of light charged particles such as protons typically yields well-localized energy deposits in segmented detector arrays, the detection of gamma rays which emerge from the reaction vertex presents significant challenges. These primarily arise from the inherently sparse and spatially distributed energy deposits resulting from the interaction mechanisms of photons with the scintillator material (see Fig. 1) [9].

At photon energies below approximately 300 keV, the photoelectric effect dom-

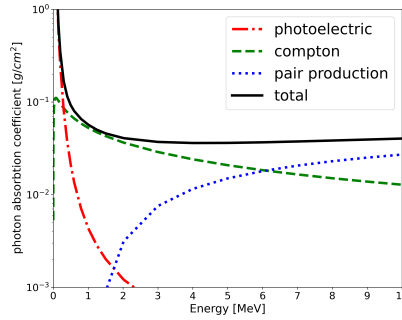


Figure 1: Photon absorption coefficients in CsI in the range from 100 keV to 10 MeV with data from XCOM database [10].

inates the interaction cross-section in the CALIFA detector material (CsI(Tl)). As the photon energy increases, Compton scattering becomes the predominant process. For photon energies exceeding the pair production threshold ($E_\gamma > 2m_e c^2 \approx 1.022 \text{ MeV}$), electron-positron pair creation becomes possible and is the dominant interaction mechanism above $E_\gamma \approx 6 \text{ MeV}$. Compton scattering broadens the clustering by the deflection of the incident gamma ray. According to the Klein-Nishina formula, the scattering is predominantly forward-focused for moderate to high photon energies [11], leading to additional clusters in neighboring crystals. At high photon energies, the dominant interaction mechanism in the detector

material is pair production (see Fig. 1), in which the incident photon converts into an electron-positron pair during the initial interaction. The subsequent annihilation of the positron results in the emission of two additional gamma photons, each with an energy of 511 keV. These secondary photons often escape the initial interaction site, leading to a significant fraction of the incident photons energy being deposited in multiple detector elements.

For gamma rays emitted by nuclei at rest, this behavior gives rise to well-defined single- and double-escape peaks in the recorded energy spectra – corresponding to the escape of one or both 511 keV photons, respectively – if these photons exit the cluster volume without interaction.

In experiments involving relativistic ion beams, such as those exploited at R3B, Doppler broadening significantly affects the observed spectral features, including the single- and double-escape peaks. Moreover, for primary gamma rays with energies well above the pair production threshold ($E_\gamma > 2m_e c^2$), both the electron and the positron produced in the initial interaction are subject to substantial energy loss via Bremsstrahlung. These effects contribute to a complex and highly non-trivial interaction pattern of gamma rays within the segmented detector system.

2.2. Data Structure and geometrical R3B Clustering Algorithm

The fundamental data entity in the analysis is a hit, defined as a discrete signal recorded by an individual detector segment at a specific time. To suppress contributions from low-energy background, only signals exceeding a predefined energy threshold are registered. In the present analysis, this threshold was set to 100 keV.

In the standard data acquisition (DAQ) configuration, all CALIFA detector hits occurring within a $\pm 4\mu\text{s}$ time window are grouped into a single event. Each individual hit i in one of the detector crystals is represented by a data structure containing the calibrated energy deposit E_i , the polar angle θ_i , the azimuthal angle ϕ_i , and a time stamp t_i , which is synchronized using the White Rabbit

89 Precision Time Protocol [12].

90 In the geometrical R3B clustering approach, the time information t_i is not uti-

91 lized during the spatial reconstruction of clusters.

92 The initial stage of the clustering algorithm begins by sorting all hits in de-

93 scending order of energy. A user-defined geometric condition, typically a cone

94 emerging from the central target point with an aperture of 0.25 rad, is applied.

95 This value has been found to provide an optimal compromise between compact

96 high-energy clusters from light charged particles and more diffuse gamma-ray

97 showers.

98 The hit with the highest energy defines the seed or center of the first cluster. The

99 algorithm then iterates through the remaining hits and includes each hit to the

100 current cluster if it sits within the specified cone relative to the seed direction.

101 Once the list is fully processed for the current cluster, the next highest-energy

102 unassigned hit becomes the seed of a new cluster. This procedure repeats until

103 no unassigned hits remain.

104

105 *2.3. Simulation Setup*

106 Simulated datasets are used to evaluate and compare the performance of

107 the clustering algorithms presented in this work. A geometrical model of the

108 detector, closely matching the experimental setup, was implemented within

109 the R3BROOT framework. The simulation employs a GEANT4-based Monte

110 Carlo [13] back-end, which accounts for all relevant secondary interaction pro-

111 cesses. This approach enables realistic modeling of energy deposition and pro-

112 vides access to ground-truth labels for each individual interaction.

113

114 The CALIFA detector geometry used in the simulation corresponds to the

115 configuration implemented in early 2024. At that time, the iPhos region (polar

116 angles $19^\circ - 43^\circ$) was fully instrumented, while only the forward half of the

117 Barrel region ($43^\circ - 87^\circ$) was active. The forward-most CEPA region ($7^\circ - 19^\circ$)

118 was not yet equipped.

119 Gamma-ray energies were sampled from a uniform distribution between 0.3 MeV
 120 and 10 MeV. The interaction of the primary gamma rays with the CsI(Tl) scin-
 121 tillation material was modeled using Geant4.
 122 To emulate realistic event topologies of signal and background, three gamma
 123 rays were generated per event, resulting in multiple detector hits. Timing infor-
 124 mation was coarsely simulated by assigning to each primary gamma a random
 125 emission time within the $\pm 4 \mu\text{s}$ event window. The corresponding hit times were
 126 then Gaussian-smeared with a standard deviation of 200 ns to reflect the timing
 127 spread of the electronic signal of slow CsI(Tl) scintillator crystals.
 128 Event selection is limited to cases in which all three gamma rays are—at least
 129 partially—detected within the geometrical acceptance of the CALIFA detector,
 130 which only partially encloses the target region. For gamma rays that deposit
 131 only a fraction of their energy in the detector volume, the corresponding true
 132 energy is adjusted to reflect only the energy actually deposited in CALIFA.
 133 The resulting dataset was split into training and test subsets, comprising 13,000
 134 and 7,000 events, respectively.

135 *2.4. Performance Metrics*

136 To quantitatively assess the performance of the clustering algorithms pre-
 137 sented in this work, a set of four custom metrics was defined. Three of these
 138 are event-based, while an optional fourth metric evaluates clustering quality on
 139 a per-cluster basis:

- 140 • **True Positive (TP)**: All hits in an event are correctly assigned to their
 141 respective clusters.
- 142 • **False Positive (FP)**: At least one hit in an event is incorrectly merged
 143 into a cluster it does not belong to.
- 144 • **False Negative (FN)**: At least one hit is not merged into its true cluster
 145 and instead forms a spurious cluster.
- 146 • **False Mixed (FM)**: An event is classified as false mixed if it contains

both FP and FN characteristics – i.e., at least one hit is incorrectly merged,
and at least one true cluster is partially reconstructed.

In addition, a cluster-based metric is defined:

- **Well Reconstructed (WR):** The ratio of correctly reconstructed clusters to the total number of true clusters in the dataset.

These metrics allow a comprehensive evaluation of clustering accuracy, robustness, and failure modes.

Special attention must be given to the false negative rate, which is closely associated with the complex interaction pattern in the segmented detector. These processes produce widely spread hits that cannot be merged using the geometrical R3B clustering method, thereby motivating the development of a multi-layer perceptron architecture to improve clustering performance at the boundaries (see Subsection 2.6).

2.5. Agglomerative Clustering

To incorporate temporal information into the clustering process—unlike the geometrical R3B algorithm, which omits it—a generic, well-established method was adopted: agglomerative clustering [7] as implemented in the `SciPy` library [14]. This unsupervised learning algorithm enables flat clustering based on hierarchical linkage with a user-defined threshold.

Each hit was mapped into spherical coordinates (θ, ϕ, r) , where the radial component r encodes time information. To ensure non-negative radii, the acquisition time window of $\pm 4 \mu\text{s}$ was shifted by $+4.5 \mu\text{s}$. The Ward linkage criterion [15], which minimizes intra-cluster variance, was employed as the distance metric.

The threshold parameter was optimized to yield the best performance according to the custom-defined *true positive* (TP) and *well reconstructed* (WR) metrics. As shown in Table 1, the agglomerative clustering algorithm demonstrates improved performance both on an event level (true positive rate) and on a cluster

level (correctly reconstructed clusters) compared to the geometrical R3B clustering. However, this improvement is accompanied by an increased false negative rate, indicating that the algorithm tends to under-merge hits near the edges of clusters. This limitation motivated the development and application of an edge detection neural network, which is introduced in the following subsection.

2.6. Edge Detection Neural Network

To enhance the clustering performance, particularly at the boundaries of hit distributions, a multi-layer perceptron architecture was developed using the PyTorch library [16] to perform pairwise classification of detector hits. This model is applied either to individual raw hits or to hits pre-clustered via agglomerative clustering, on an event-by-event basis.

The model takes 12 input features for each hit pair (i, j) : absolute values of energy (E_i, E_j) , polar angle (θ_i, θ_j) , azimuthal angle (ϕ_i, ϕ_j) , and time (t_i, t_j) . Additionally, four differential features are computed: $\Delta E = |E_i - E_j|$, $\Delta\theta = |\theta_i - \theta_j|$, $\Delta\phi = |\phi_i - \phi_j|$, and $\Delta t = |t_i - t_j|$. These differential inputs are helpful for training stability and convergence with our limited model sizes tested. In particular, $\Delta\phi$ resolves the discontinuities caused by the periodicity of the azimuthal angle (e.g., distinguishing between $\phi = 355^\circ$ and $\phi = 5^\circ$), which would otherwise introduce large erroneous differences in angular comparisons.

Of the 12 features, only the hit time is normalized to the $[0, 1]$ interval; all other values are used in their native physical units. The neural network architecture takes the 12-dimensional input vector and passes it through a fully connected feed-forward network with one hidden layer of 10^3 nodes, followed by a rectifier linear unit activation function (ReLU) [17]. Two additional hidden layers, each with 10^2 nodes, are applied sequentially. The output layer consists of a single node with a sigmoid activation, yielding a score in the interval $[0, 1]$, where values close to 1 indicate that the hits (or clusters) are likely to originate from the same event cluster.

Training is performed using the binary cross-entropy loss function [18, 19]

205 and stochastic gradient descent (SGD) [20] with a fixed learning rate of 5×10^{-3} .
 206 Given the moderate size of the training dataset, full-batch training is employed
 207 without mini-batching. The model is trained for 8×10^4 epochs. After training, a
 208 threshold is applied to the prediction scores to classify hit pairs. This threshold
 209 is tuned to optimize the performance across all defined metrics, as described in
 210 Subsection 2.4. Final clusters are then formed by grouping all connected hit
 211 pairs based on the predicted associations.

212 The edge detection NN was implemented and tested in three configurations:

- 213 • **Plain Edge NN:** The model is applied directly to individual hits without
 214 any pre-clustering. All clustering is performed based solely on the NN
 215 predictions.
- 216 • **R3B + Edge NN:** The data are first clustered using the geometrical R3B
 217 clustering algorithm as an initial clean-up step. For each resulting cluster,
 218 an energy-weighted center of mass is calculated, replacing individual hits.
 219 The NN is then trained exclusively on false negative cases, i.e., events
 220 where reconstructed clusters exhibit detached hits. In application, the
 221 geometrical R3B clustering is first applied to the test data, followed by
 222 the NN to refine cluster boundaries and reduce the false negative rate as
 223 clean-up step.
- 224 • **Agglo + Edge NN:** This strategy mirrors the R3B+Edge approach,
 225 with the key difference that time information is incorporated. As in the
 226 R3B+Edge model, the NN is trained on false negative cases to perform
 227 a final clean-up step after pre-clustering the hits using the agglomerative
 228 clustering algorithm described in the previous subsection. The signifi-
 229 cant reduction of the false negative rate achieved by the clean-up step in
 230 the Agglo+Edge implementation is demonstrated in Figure 2, which com-
 231 pares the reconstructed energy spectra from simulations of mono-energetic
 232 2.1 MeV gamma events using the geometrical R3B clustering and the Ag-
 233 glo+Edge method.

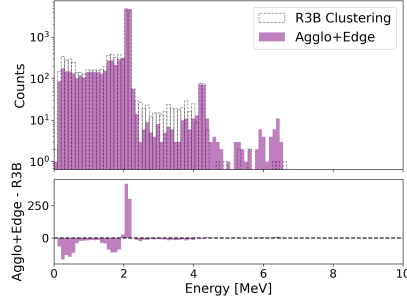


Figure 2: Reconstructed gamma energy spectrum from simulated events, each consisting of three 2.1 MeV gamma photons emitted from the target point. The upper panel shows the comparison between the geometrical R3B clustering and the Agglo+Edge method. The lower panel displays the bin-by-bin count difference between the two approaches. The Agglo+Edge model demonstrates a significant improvement by successfully reattaching escaped hits, notably in cases where sparse energy deposits around 1.6 MeV and 0.5 MeV result from pair production and subsequent annihilation processes of the original gamma photons. This clean-up step leads to a marked reduction in false negatives compared to the geometrical R3B clustering.

3. Discussion

Clustering Model	TP(†)	FP(‡)	FN(‡)	FM(‡)	WR(†)
Geometrical R3B Clustering	60.6	5.3	25.2	8.9	80.4
Agglomerative Clustering	62.8	3.3	32.0	1.9	84.1
Edge Clustering (no time)	63.4±0.3	7.2±0.3	24.8±0.7	4.6±0.1	82.4±0.1
Edge Clustering (with time)	74.7±0.5	3.4±0.6	20.5±1.3	1.4±0.1	89.2±0.1
R3B + Edge (no time)	67.4±0.3	8.5±0.3	16.0±0.4	8.0±0.3	82.2±0.1
Agglo + Edge (with time)	81.3±0.3	5.1±0.0	12.2±0.3	1.5±0.1	91.0±0.1

Table 1: Summary of performance metrics as defined in Subsection 2.4, evaluated for the different clustering algorithms. The models *Geometrical R3B Clustering*, *Edge Clustering (no time)*, and *R3B + Edge (no time)* utilize only angular and energy information on a per-hit basis for cluster reconstruction. In contrast, *Agglomerative Clustering*, *Edge Clustering (with time)*, and *Agglo + Edge (with time)* additionally incorporate time-of-hit information into the clustering process. Uncertainties reported for the four edge detection neural network variants correspond to the standard deviation of the results obtained from ten independent training runs.

The results of this study are summarized in Table 1, organized according to increasing levels of reconstruction complexity. For completeness, the previously

237 obtained results from the comparison between the "baseline" geometrical R3B
 238 clustering algorithm and the agglomerative model are also included.
 239 The agglomerative model shows improved performance over the R3B baseline
 240 in terms of both event-level true positives (TP) and cluster-level (WR) val-
 241 ues. However, it exhibits inferior performance with respect to the false negative
 242 (FN) rate, indicating a tendency to miss relevant hits during reconstruction.
 243 This limitation motivated the development of an Edge Detection Neural Net-
 244 work, initially evaluated as a standalone clustering algorithm and subsequently
 245 integrated into the agglomerative framework, yielding the combined model de-
 246 noted as *Agglo + Edge*.
 247 The *Agglo + Edge* model demonstrates superior performance across all evalu-
 248 ated metrics, achieving an overall correct reconstruction rate of 81.3%, signifi-
 249 cantly outperforming the *Geometrical R3B Clustering* algorithm, which reaches
 250 60.6%.
 251 A visual representation of an example event, contrasting the incorrectly merged
 252 hits from the geometrical R3B clustering with the correctly reconstructed clus-
 253 tering using the Agglo+Edge model, is shown in Figure 3.

254

255 To further explore the capabilities of neural network-based clustering ap-
 256 proaches, two additional models were evaluated: a standalone *Edge Detection*
 257 *Neural Network* and a hybrid approach combining *Geometrical R3B Clustering*
 258 with edge-based postprocessing (*R3B + Edge*). Notably, both of these mod-
 259 els operate without incorporating time-of-hit information, similar to the R3B
 260 baseline. Nonetheless, both outperform the *Geometrical R3B Clustering*, under-
 261 scoring the potential of edge-based neural network models for improving cluster
 262 reconstruction in high-granularity detector systems.

263 The edge detection NNs presented here represent a special case of Graph Neural
 264 Networks (GNNs) [21], which, along with the more sophisticated transformer
 265 models [22, 23], have seen widespread adoption in particle physics over the past
 266 five years [24–26]. Interestingly, for this application, using an unsupervised
 267 learning algorithm (agglomerative clustering) to first define a graph structure

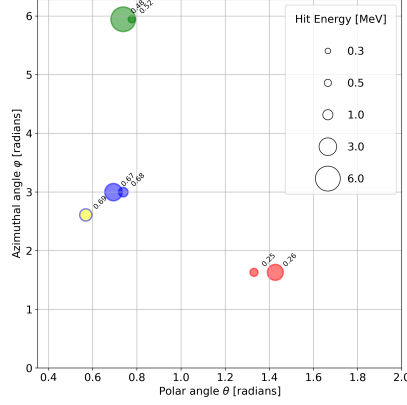


Figure 3: Example of a simulated event involving three primary gamma photons, illustrating the performance difference between the Agglo+Edge clustering method and the geometrical R3B clustering approach. Each marker represents a detected hit, plotted as a function of the polar angle θ and the azimuthal angle φ . The edge color of each circle indicates the true cluster assignment (ground truth), while the fill color denotes the cluster assignment according to the geometrical R3B clustering. The size of each circle reflects the energy deposited in the detector segment. Numbers adjacent to the hits represent the normalized hit times. In this event, the geometrical R3B clustering incorrectly assigns the hit at ($\theta \approx 0.6$ rad, $\varphi \approx 2.7$ rad), with a normalized time of 0.69 (blue edge, yellow fill), to a separate cluster, resulting in a *False Negative* (FN). In contrast, the Agglo+Edge method correctly assigns all hits to their respective clusters.

presented a powerful inductive bias for our application which much improved
our results over the standalone edge-NN.

4. Outlook

The results presented in the previous section clearly demonstrate that high-level machine learning approaches, such as the Edge Detection NN, can significantly enhance the accuracy of cluster reconstruction. These models not only reduce distortions in the measurement process but also exhibit increased sensitivity to low-statistics reactions – an important feature for experiments targeting rare processes.

It is noteworthy that even the models, which do not utilize time-of-hit infor-

278 mation (similarly to the *Geometrical R3B Clustering*), outperform the baseline
 279 method. This underscores the general effectiveness of neural network-based
 280 methods in extracting structural features from detector data.
 281 The inclusion of time-of-hit information proves to be a critical factor for enhanc-
 282 ing clustering performance. As this observable is typically available for CALIFA
 283 at R3B, the results of this study support the recommendation to incorporate it
 284 into the reconstruction pipeline wherever possible.
 285 Furthermore, these findings are intended to encourage broader adoption of ad-
 286 vanced machine learning techniques by experimental groups, particularly in se-
 287 tups involving highly granular detectors. Such tools offer substantial perfor-
 288 mance benefits and can support more precise event reconstruction.
 289 One inherent limitation of the applied approach is its inability to correct for
 290 overly aggressive pre-clustering. In particular, false positive assignments in-
 291 troduced during the initial stage cannot be mitigated during the subsequent
 292 clean-up step by the edge-NN. This limitation is visible in Fig. 2, where a slight
 293 excess of reconstructed counts at $E_{reco} \approx 6.3$ MeV is observed, likely indicating
 294 erroneous merging of unrelated hits due to excessive clustering. Despite this
 295 artifact, the high false negative rate – exceeding the false positive rate by more
 296 than a factor of five in the baseline R3B clustering (see Table 1) – motivated
 297 the development of a clustering strategy that prioritizes the recombination of
 298 hits to form complete clusters.
 299 Subsequent work could consider also adding a subsequent cluster splitting step in
 300 an end-to-end optimizable algorithm. Although, in principle, transformers could
 301 learn the graph structure directly from hit distributions, initial tests showed
 302 limited performance, highlighting an opportunity for the community to further
 303 develop combined machine learning-based reconstruction methods.
 304 From a computational standpoint, both the geometrical R3B clustering and the
 305 agglomerative clustering algorithms scale quadratically with the number of in-
 306 put hits, exhibiting a time complexity of $\mathcal{O}(N^2)$, where N denotes the number
 307 of detector hits per event. The combined methods –R3B + Edge and Agglo +
 308 Edge – induce additional computational overhead due to the Edge Detection

Neural Network (NN) employed in the second stage. The current network architecture comprises three fully connected hidden layers with up to 10^3 neurons each, resulting in large matrix operations that dominate the runtime for typical events with $N \sim \mathcal{O}(10^2)$. Consequently, future work will focus on optimizing the Edge Detection NN by significantly reducing the model size to enable faster execution while improving performance compared to the conventional geometrical R3B clustering.

Additionally, transformer-based models [22] – capable of analyzing full event topologies – may offer further improvements in clustering accuracy by capturing complex, global features.

Acknowledgements

The work was supported by BMBF 05P24WO2 and Excellence Cluster ORIGINS from the DFG (Excellence Strategy EXC-2094-390783311). It was made possible through the close collaboration of experts from different disciplines within the Cluster of Excellence ORIGINS [27].

Declaration of generative AI and AI-assisted technologies in the writing process.

During the preparation of this work the authors used AI-assisted tools, including ChatGPT (OpenAI) and Gemini (Google), in order to improve the readability and language of the article. After using this tools, the authors reviewed and edited the content as needed and take full responsibility for the content of the published article.

- [1] N. Kalantar-Nayestanaki and C. Scheidenberger, Experiments at the Interface of Nuclear, Atomic, and Hadron Physics with FRS at GSI and Super-FRS at FAIR, Nuclear Physics News 34 (2024) 21–26.
- [2] Y. Leifels, Status and physics perspectives of FAIR, Il Nuovo Cimento 100 (2025) 48.

- 336 [3] D. Cortina-Gil, H. Alvarez-Pol, T. Aumann et al., CALIFA, a Dedicated
337 Calorimeter for the R3B/FAIR, Nuclear Data Sheets 120 (2014) 99–101.
- 338 [4] H. Alvarez-Pol, N. Ashwood, T. Aumann et al., Performance analysis for
339 the CALIFA Barrel calorimeter of the R3B experiment, Nuclear Instru-
340 ments and Methods in Physics Research Section A: Accelerators, Spec-
341 trometers, Detectors and Associated Equipment 767 (2014) 453–466.
- 342 [5] T. Le Bleis, M. Bendel, R. Gernhäuser et al., A Digital Readout for CAL-
343 IFA, [https://www.mll-muenchen.de/forschung/instrumentierung/](https://www.mll-muenchen.de/forschung/instrumentierung/califa_14.pdf)
344 [califa_14.pdf](https://www.mll-muenchen.de/forschung/instrumentierung/califa_14.pdf), 2014. Accessed: 2025-04-06.
- 345 [6] D. Bertini, R3BRoot, simulation and analysis framework for the R3B
346 experiment at FAIR, in: Journal of Physics: Conference Series, volume
347 331, IOP Publishing, 2011, p. 032036.
- 348 [7] F. Nielsen, Hierarchical Clustering, Springer International Publishing,
349 Cham, 2016, pp. 195–211.
- 350 [8] M.-C. Popescu, V. E. Balas, L. Perescu-Popescu et al., Multilayer percep-
351 tron and neural networks, WSEAS Transactions on Circuits and Systems
352 8 (2009) 579–588.
- 353 [9] H. Kolanoski and N. Wermes, Teilchendetektoren, Springer, 2016.
- 354 [10] S. Seltzer, XCOM-Photon Cross Sections Database, NIST Standard Ref-
355 erence Database 8, <http://www.nist.gov/pml/data/xcom/index.cfm>,
356 2010. Accessed: 2025-04-10.
- 357 [11] O. Klein and Y. Nishina, Über die Streuung von Strahlung durch freie
358 Elektronen nach der neuen relativistischen Quantendynamik von Dirac,
359 Zeitschrift für Physik 52 (1929) 853–868.
- 360 [12] M. Lipiński, T. Włostowski, J. Serrano et al., White rabbit: A PTP ap-
361 plication for robust sub-nanosecond synchronization, in: 2011 IEEE Inter-
362 national Symposium on Precision Clock Synchronization for Measurement,
363 Control and Communication, IEEE, 2011, pp. 25–30.

- [13] S. Agostinelli, J. Allison, K. a. Amako et al., GEANT4a simulation toolkit, Nuclear instruments and methods in physics research section A: Accelerators, Spectrometers, Detectors and Associated Equipment 506 (2003) 250–303.
- [14] P. Virtanen, R. Gommers, T. E. Oliphant et al., SciPy 1.0: fundamental algorithms for scientific computing in Python, Nature methods 17 (2020) 261–272.
- [15] F. Nielsen and F. Nielsen, Hierarchical clustering, Introduction to HPC with MPI for Data Science (2016) 195–211.
- [16] S. Imambi, K. B. Prakash and G. Kanagachidambaresan, Pytorch, Programming with TensorFlow: solution for edge computing applications (2021) 87–104.
- [17] A. F. Agarap, Deep learning using rectified linear units (relu), arXiv preprint arXiv:1803.08375 (2018).
- [18] S. Mannor, D. Peleg and R. Rubinstein, The cross entropy method for classification, in: Proceedings of the 22nd international conference on Machine learning, 2005, pp. 561–568.
- [19] P.-T. De Boer, D. P. Kroese, S. Mannor et al., A tutorial on the cross-entropy method, Annals of operations research 134 (2005) 19–67.
- [20] D. Newton, R. Pasupathy and F. Yousefian, Recent trends in stochastic gradient descent for machine learning and Big Data, in: 2018 Winter Simulation Conference (WSC), IEEE, 2018, pp. 366–380.
- [21] P. W. Battaglia, J. B. Hamrick, V. Bapst et al., Relational inductive biases, deep learning, and graph networks, arXiv preprint arXiv:1806.01261 (2018).
- [22] A. Vaswani, N. Shazeer, N. Parmar et al., Attention is all you need, Advances in neural information processing systems 30 (2017).

- 390 [23] X. Amatriain, A. Sankar, J. Bing et al., Transformer models: an introduc-
391 tion and catalog, arXiv preprint arXiv:2302.07730 (2023).
- 392 [24] G. DeZoort, S. Thais, J. Duarte et al., Charged particle tracking via edge-
393 classifying interaction networks, Computing and Software for Big Science
394 5 (2021) 1–13.
- 395 [25] X. Ju, D. Murnane, P. Calafiura et al., Performance of a geometric deep
396 learning pipeline for HL-LHC particle tracking, The European Physical
397 Journal C 81 (2021) 1–14.
- 398 [26] S. Van Stroud, P. Duckett, M. Hart et al., Transformers for Charged
399 Particle Track Reconstruction in High Energy Physics, arXiv preprint
400 arXiv:2411.07149 (2024).
- 401 [27] Cluster of Excellence ORIGINS, Cluster of excellence origins, [https://](https://www.origins-cluster.de)
402 www.origins-cluster.de, 2025. Accessed: 2025-05-03.